

PAPER

## Type-I ELM power loads on the closed outer divertor targets in the HL-2A tokamak

To cite this article: J.M. Gao *et al* 2021 *Nucl. Fusion* **61** 066024

View the [article online](#) for updates and enhancements.

### You may also like

- [Integration of a radiative divertor for heat load control into JET high triangularity ELMy H-mode plasmas](#)  
C. Giroud, G. Maddison, K. McCormick et al.
- [Progress on the application of ELM control schemes to ITER scenarios from the non-active phase to DT operation](#)  
A. Loarte, G. Huijsmans, S. Futatani et al.
- [ELM behavior in ASDEX Upgrade with and without nitrogen seeding](#)  
L. Frassinetti, M.G. Dunne, M. Beurskens et al.

# Type-I ELM power loads on the closed outer divertor targets in the HL-2A tokamak

J.M. Gao<sup>1,\*</sup>, L.Z. Cai<sup>1</sup>, X.L. Zou<sup>2</sup>, T. Eich<sup>3</sup> , J. Adamek<sup>4</sup> , C.Z. Cao<sup>1</sup>, Z.H. Huang<sup>1</sup>, X.Q. Ji<sup>1</sup>, M. Jiang<sup>1</sup>, L. Liu<sup>1</sup>, J. Lu<sup>1</sup>, Y. Liu<sup>1</sup>, Z.B. Shi<sup>1</sup>, A.J. Thornton<sup>5</sup>, N. Wu<sup>1</sup> , G.L. Xiao<sup>1</sup>, M. Xu<sup>1</sup>, L.W. Yan<sup>1</sup>, L.M. Yu<sup>1</sup> , D.L. Yu<sup>1</sup>, Q.W. Yang<sup>1</sup>, W.L. Zhong<sup>1</sup> and the HL-2A Team<sup>1</sup>

<sup>1</sup> Southwestern Institute of Physics, Chengdu 610041, China

<sup>2</sup> CEA, IRFM, Saint-Paul-lez-Durance F-13108, France

<sup>3</sup> Max-Planck-Institut für Plasmaphysik, Garching, Germany

<sup>4</sup> Institute of Plasma Physics of the CAS, Prague, Czech Republic

<sup>5</sup> CCFE, Culham Science Centre, Oxfordshire OX14 3DB, United Kingdom of Great Britain and Northern Ireland

E-mail: [gaojm@swip.ac.cn](mailto:gaojm@swip.ac.cn)

Received 9 December 2020, revised 29 March 2021

Accepted for publication 1 April 2021

Published 5 May 2021



CrossMark

## Abstract

The HL-2A tokamak has a very closed divertor geometry, and a new infrared camera has been installed for high resolution studies of edge-localized mode (ELM) heat load onto the outer divertor targets. The characteristics of power deposition patterns on the lower outer divertor target plates during ELMs are systematically analysed with infrared thermography. The ELM energy loss is in the range of 3%–8% of the total plasma stored energy. The peak heat flux on the outer divertor targets during ELMs currently achieved in HL-2A is about  $1.5\text{--}3.2\text{ MW m}^{-2}$ , the wetted area is about  $0.5\text{--}0.7\text{ m}^2$ , and the corresponding integrated power decay length at the midplane is about  $25\text{--}40\text{ mm}$ . The rise time of the ELM power deposition is in the range of about  $100\text{ }\mu\text{s}$  to  $400\text{ }\mu\text{s}$ , and the decay time is typically 1.5 to 4 times longer than the corresponding rise time. Convective transport along open field lines during the ELM rise phase from the midplane towards the divertor targets is implied due to the correlation of parallel transport time in the scrape-off layer (SOL) and ELM power rise time. The peak ELM energy fluence is compared with those predicted by models and with experimental data from JET, ASDEX Upgrade, MAST, and COMPASS. The results, as a whole, show a good agreement.

Keywords: closed divertor geometry, ELM power deposition, peak ELM energy fluence

(Some figures may appear in colour only in the online journal)

## 1. Introduction

Operation in H-mode is considered to be the reference scenario for next step tokamak devices, such as ITER [1–3]. The H-mode plasmas are affected by quasi-periodic MHD instabilities occurring at the edge transport barrier region named edge-localized modes (ELMs) [4, 5]. The ELM causes a sudden crash of the transport barrier with transient releases of energy and particles into the scrape-off layer (SOL) and

eventually moves towards the divertor [6–8]. The resulting high heat load deposited onto the divertor targets may pose a serious threat to the devices. Therefore, understanding the divertor heat load patterns during ELMs is an important issue for handling the high energy flux. Considerable efforts have been dedicated to understand the behaviour of divertor heat flux during ELMs in JET-C [9], JET-ILW [10], ASDEX Upgrade [11], DIII-D [12], EAST [13], and so on. It is found that during ELMs about 1%–30% of the plasma stored energy is released within a few hundred microseconds towards the

\* Author to whom any correspondence should be addressed.

divertor, and the power decay length (deposited area) is only tens of millimeters. Extrapolation of the multi-machine experimental results to ITER indicates the parallel peak ELM energy fluence is 2.5–7.5 MJ m<sup>-2</sup> for the intermediate ITER operation at 7.5 MA and 2.65 T [14]. It is larger than the material limit for ELM peak divertor thermal impact. Thus, ELM control techniques, such as resonant magnetic perturbations and impurity seeding, could be required for next step tokamak devices.

The ELM mitigation requirements are based on extrapolations which depend on models. Based on experimental findings on JET, ASDEX Upgrade, and MAST, a model was put forward, from here on referred to as the Eich model [14]. The Eich model proposes that parallel ELM energy densities scale with pedestal pressure, and the predictions are compared against a multi-machine dataset, including measurements from JET, ASDEX Upgrade, and MAST [14]. The scaling prediction was recently tested on COMPASS [15] and DIII-D [16] with a good agreement.

The HL-2A tokamak has a very closed divertor geometry, and the outer divertor target plates are monitored with a fast infrared (IR) camera. A set of ELMy H-mode discharges have been performed during the HL-2A divertor campaign with an optimized divertor configuration, so that the outer strike point is located in the field of view of the IR camera [17, 18]. The power deposition characteristics of type-I ELMs with frequency from 70 Hz to 200 Hz are investigated with the IR camera. The energy loss during ELMs currently achieved in HL-2A is in the range of 3% to 8% of the total plasma stored energy; as a result, the peak heat flux on the outer divertor targets is about 1.5–3.2 MW m<sup>-2</sup> and the integrated power decay length at the midplane is about 25–40 mm. Values of 25–40 mm seem to be substantially larger than that on many current devices, but this is roughly consistent with scaling [19] and the low plasma current values in these HL-2A experiments. During the ELM cycle, the decay time is much larger than the rise time, and the rise time is comparable to the parallel transport time in the SOL. Finally, the ELM energy density profiles and peak ELM energy density values are compared to the scaling predictions from ASDEX Upgrade, JET, MAST, and COMPASS.

The rest of this paper is organized as follows. In section 2, a brief description of the HL-2A divertor configuration, ELM diagnostic systems, and the ELMy H-mode plasma database is given. Characteristics of the ELM power load on the outer divertor targets are reported in section 3. Section 4 presents the energy transport in the SOL during ELMs. The ELM energy density profiles and the peak ELM energy fluence are compared to the scaling predictions from JET, ASDEX Upgrade, MAST, and COMPASS in section 5. Finally, a summary and conclusions are presented in section 6.

## 2. Experimental arrangement

### 2.1. Divertor configuration

The HL-2A tokamak (major radius  $R = 1.65$  m and minor radius  $a = 0.4$  m) is operated in the lower single-null (LSN) divertor configuration with the ion magnetic

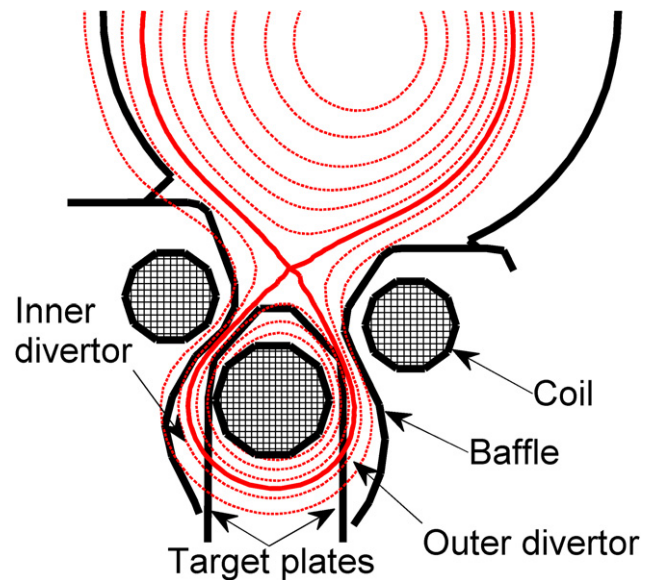


**Figure 1.** Coils, baffles, and target plates form the very closed lower divertor of HL-2A.

gradient drift towards the X-point. This device has a very closed divertor geometry, where a closely spaced coil triplet with zero net current is used to produce the divertor configuration [17], as shown in figure 1. Additional (‘multipole compensation’) coils are added to cancel even the residual far-field of the two (symmetrically top and bottom) divertor triplets over the main plasma region, so that core flux surfaces are close to perfectly circular.

### 2.2. ELM diagnostics

Diagnostic measurements on HL-2A that are capable of sampling during ELM events provide the heat flux on the outer divertor target plates,  $D_\alpha$  emission in the outer divertor chamber, electron density and temperature in the pedestal, and total radiation in the main plasma and the outer divertor region. A poloidal cross section, which shows the locations of these diagnostics and the plasma equilibrium shape used in these experiments, is given in figure 2(a).

The divertor heat flux is calculated from the evolution of surface temperature on the target plates, measured by an IR camera [18]. The IR camera contains gallium arsenic sensors operating in 8–9.4  $\mu\text{m}$  spectral range, allowing surface temperature from  $-40$  °C to 1000 °C to be measured. An oblong opening on the baffle is cut and thus the outer divertor target plates are monitored directly by the IR camera through a ZnSe vacuum window, as shown in figure 2(b). Note that there is no inner target IR measurement because viewing is difficult with the very closed divertor geometry. Because the divertor plates have been exposed to the plasma for more than ten years, the plate surface is polluted strongly by the plasma as shown in figure 2(b). Thus, a new  $8 \times 20$  cm target graphite tile has taken the place of the old copper plates recently, but the region of  $6 \times 15$  cm can be measured by the IR camera due to the baffle shield, as shown in figure 2(c). In order to investigate the characteristics of the ELM power deposition patterns, the IR camera was optimized to have a best field of view covering the

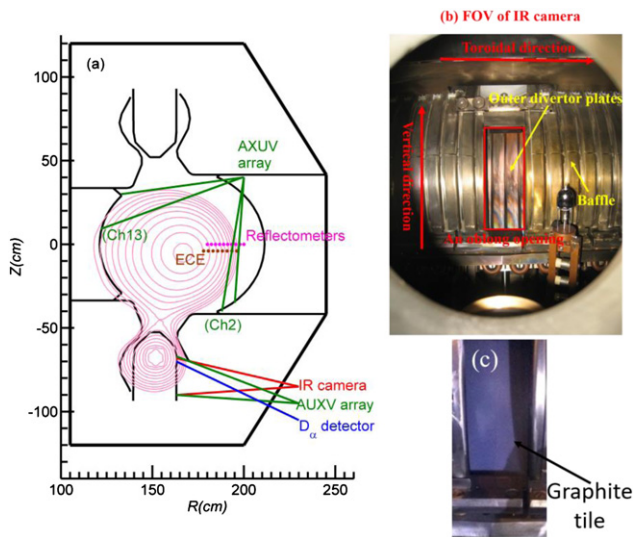


**Figure 2.** (a) The cross section of HL-2A shows a typical plasma shape used in these experiments and some of the diagnostics used in the ELM analysis, (b) the field of view of the IR camera; the outer divertor plates are monitored by the IR camera through an oblong window on the baffle, and (c) the field of view of IR camera with a reduced array size covering the new graphite target. The lines of sight labelled by ‘Ch2’ and ‘Ch13’ are used for energy transport in the SOL in figure 7.

strike point zones, and to use a reduced array size with a 4 kHz sampling rate to resolve the ELM. The spatial resolution is as small as about 2 mm. The thickness of the graphite tile is about 1.5 cm, and the plasma pulse is about 2 s in the HL-2A experiments; a numerical 2D heat flux calculation (making assumptions on the energy deposition toroidal symmetry) is carried out with the measured time evolution of the surface temperature. A duration of about 10 min between two shots of plasma experiments guarantees the graphite tile returns back to the ambient temperature. There is a thin surface layer at the top of the target surface due to the redeposition of impurity; and the heat flux value calculated from IR measurements depends strongly on the presence of a thin surface layer with low thermal conductivity and low adherence [9]. Therefore, a heat transmission layer at the top of the target surface is also introduced in the heat flux calculation [9]. Such developments the temperature measurement and heat flux calculation more accurate.

$D_\alpha$  emission in the lower outer divertor is measured with a fast  $D_\alpha$  emission detector at a 100 kHz rate [17]. Two poloidal arrays of fast absolute extreme ultraviolet (AXUV) photodiode detectors are employed for estimating the total plasma radiated power during ELMs along multiple chordal views in the main plasma chamber and lower outer divertor. Each AXUV array contains 16 channels resulting in a spatial resolution of about 5 cm in the main plasma and of about 1.5 cm in the divertor. The outer midplane density profile in the SOL and steep gradient region of the pedestal during the ELM cycle is obtained up to  $2 \times 10^{19} \text{ m}^{-3}$  from the X-mode frequency modulated continuous wave reflectometers [20]. The sampling rate of the density profile can be as high as 40 kHz, while spatial resolution can be as small as  $\sim 1$  cm. The electron temperature in the pedestal during the ELM cycle is determined by an electron

cyclotron emission (ECE) radiometer [21]. This system has a tunable local oscillator source, and can measure the 2nd harmonic ECE frequency from 51 GHz to 142 GHz. The spatial resolution is about 1.5 cm at the toroidal field of 1.3 T and the temporal resolution is about 1  $\mu\text{s}$ .

### 2.3. Experimental data of ELMy H-mode discharges

All results reported in this paper were obtained in deuterium discharges. The LSN divertor configuration with the ion magnetic field gradient drift towards the X-point was used, and a magnetic equilibrium similar to that in figure 2 was optimized for IR measurements of the divertor target power deposition during experiments.

The main parameters for the ELMy H-mode plasmas were  $I_p = 160\text{--}200$  kA,  $B_t = 1.3\text{--}1.5$  T, and line-averaged electron density  $n_e = 2\text{--}4 \times 10^{19} \text{ m}^{-3}$ . The ELMy H-mode plasmas were achieved with the 1–1.5 MW NBI heating power. A variety of H-mode regimes with different ELM dynamics, including type-I ELMs, type-III ELMs, and grassy ELMs, were observed in HL-2A. But in order to compare against other devices, type-I ELMs with frequency from 70 Hz to 200 Hz were selected. In this contribution, 30 shots of the so-called IR-optimized ELMy H-mode discharges are chosen for power load analysis due to the combination of the complex viewing geometry, the strike zone positioning, and the desired data acquisition with the highest frequency. Some of the discharge parameters are listed in table 1. In addition, the complexity of partially detached divertor plasmas is avoided in this study because IR camera measurement at the target plate is to be meaningfully extrapolated back to the up-stream.

Figure 3 illustrates one typical HL-2A ELMy H-mode discharge. Both divertor plates are attached due to the relatively low plasma density ( $n_e/n_G \sim 0.6$ ) and the ELM frequency is around 100 Hz and very regular. ELMs cause sudden release of energy and particles from the core plasma, then the power crossing the separatrix is transported by heat conduction and convection along magnetic field lines onto the divertor plates. These ELM dynamic characteristics are observed clearly in the line-averaged electron density, plasma stored energy, plasma radiation power, and divertor heat flux, so that heat transport during ELMs and inter-ELMs can be investigated in detail with these diagnostic measurements.

## 3. Target heat load patterns during ELMs

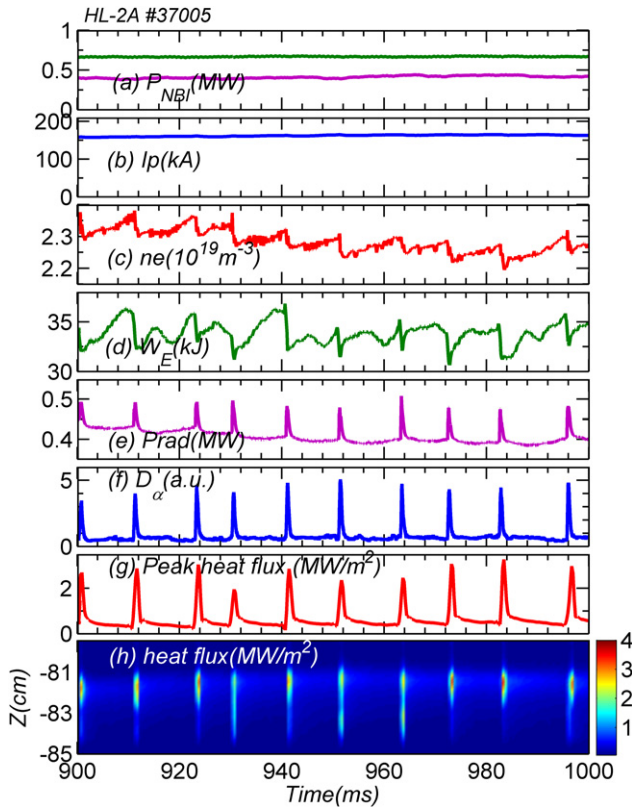
The spatial and temporal heat flux profiles are determined by IR thermography, as introduced in section 2. In order to reduce the data scatter, the profiles are obtained by averaging over seven consecutive ELMs with synchronizing the time signal with respect to the start of each single ELM. This method has been described clearly in reference [22].

### 3.1. Temporal behaviours

The time period in which an ELM deposits its energy on the divertor target is an important parameter for estimating the material limit. The ELM energy pulse to the divertor target can be divided into two phases (the rise stage and the decay

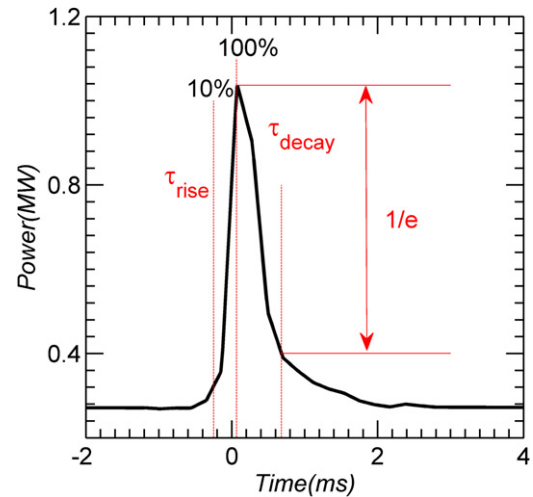
**Table 1.** Plasma conditions for the power load statistical analysis of 30 shots of type-I ELM H-mode discharges with low SOL radiation.

$I_p$ (kA)	$B_T$ (T)	$f_{ELM}$ (Hz)	$\Delta W/W_{plasma}$ (%)	$n_e/n_G$	$P_h$ (MW)
160–200	1.3–1.5	70–200	3–8	$\sim 0.5$ – $0.7$	1–1.5

**Figure 3.** Time traces of the main parameters for one typical HL-2A H-mode discharge: (a) NBI heating power (where NBI#1 in green is about 0.8 MW, NBI#2 in purple is about 0.4 MW), (b) plasma current, (c) line-averaged electron density, (d) plasma stored energy, (e) plasma radiation power, (f) divertor  $D_\alpha$  signal, (g) peak heat flux, and (h) heat flux on the outer divertor plates (the colour represents the value of heat flux in  $\text{MW m}^{-2}$ ). Note that, in order to make the effects of ELMs clearer, expanded vertical scales and suppressed zeroes are used in some of the sub-plots (c)–(e).

stage) as illustrated in figure 4. The characteristic timescale  $\tau_{\text{rise}}$  for the first phase is defined as the duration of the power increase from 10% above the initial value to 100% of the maximum measured value, and the decay time  $\tau_{\text{decay}}$  for the second phase is the duration from the peak power to 1/e decay [23]. Because  $\tau_{\text{rise}}$  and  $\tau_{\text{decay}}$  cannot be precisely estimated due to the low resampling rate of the IR camera measurement ( $\sim 4$  kHz), the error bar of about  $125 \mu\text{s}$  (half of frame time) is introduced to determine the upper and lower limits.

In figure 5(a) the power rise and decay times of a total of 30 shots for ELM discharges with a variety of ELM frequencies are plotted. The observed rise times are between about  $200 \mu\text{s}$  to  $400 \mu\text{s}$ , and the decay times are typically 1.5 to 4 times longer than the corresponding rise times. The ELM deposited energies in the power rise and decay phases are estimated with  $E = 2\pi R_{\text{div}} \iint q(s, t) ds dt$ , respectively. The ratio of the

**Figure 4.** Temporal evolution of outboard deposited power of an averaged ELM event (seven consecutive ELMs). Two phases are determined in the ELM power pulse to the divertor target.

deposited energies during the two phases varies from 2 to 5, as shown in figure 5(b). In that respect, the fraction of the energy that is deposited during the power rise phase stays below 40%, and can be as low as 20%, although the ELM deposited energy during this phase will lead to the maximum heat flux on the divertor target. These results show a similar tendency with the ELM power load temporal shape report on JET [10]. Since the rise time scales with the convective parallel time calculated with pedestal parameters [8, 23] (see section 4), so the fraction of the energy that is deposited during the power rise phase seems to depend on the pedestal plasma parameters. This implies that there might be a correlation between the dominant parallel energy transport mechanism towards the divertor along field lines and the fraction of energy deposited in the first phase of the ELM target heat fluxes [23]. We further discuss the parallel energy transport mechanism in section 4. However, the ratio of the ELM deposited energies between two phases shows no dependence on the rise time.

### 3.2. ELM power load deposition area

Periodic ELMs induce high transient heat loads onto the divertor targets. In contrast to the very localized steady state heat flux, the ELM heat load is unevenly deposited onto a comparably large area. For the measurement of the impact on the divertor target, the ELM power load deposition area is evaluated in a simple way by dividing the spatially (toroidally and radially) integrated power flux by the peak heat flux [24]. Here,  $s$  is the local coordinate along the tile surface.

$$A_{\text{wet}} = \frac{\int q_{\text{div}}(s) 2\pi R_{\text{div}} ds}{q_{\text{div}}^{\text{max}}}. \quad (1)$$

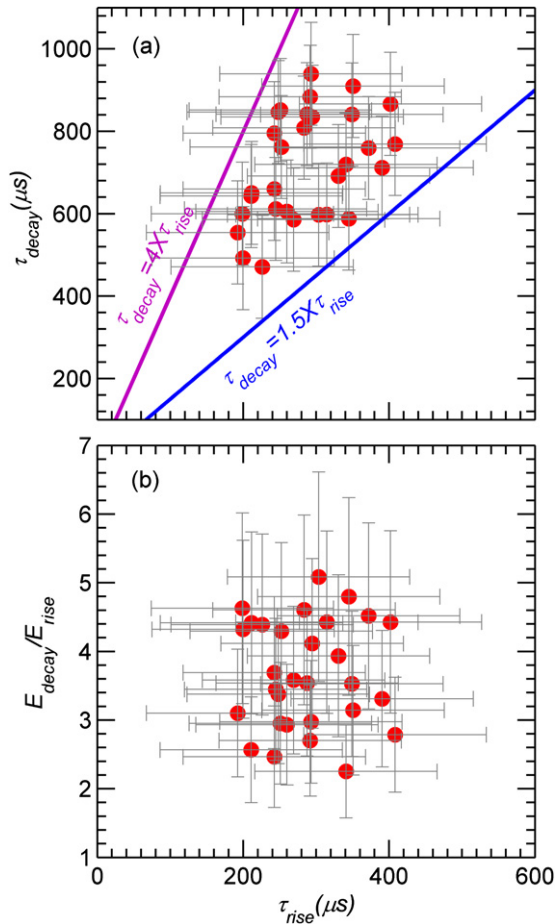


**Figure 5.** Temporal characteristics of HL-2A type-I ELMs: (a) ELM decay time versus ELM rise time, (b) ratio of the ELM energies deposited during decay and rise phases versus ELM rise time. ELM decay time is much larger than the rise time. ELM energy deposition indicates more energy is deposited in the decay phase.

In figure 6 the peak heat flux and the wetted area of the ELM peak are plotted. The peak heat flux is estimated by the maximum value of the heat flux profile. The peak value varies from about  $1.5 \text{ MW m}^{-2}$  to  $3.2 \text{ MW m}^{-2}$ , which increases with energy loss due to ELMs. The energy loss due to an ELM is determined by the sharp decrease of plasma stored energy, which is estimated with diamagnetic measurements. It is obvious that in the attached divertor regime the energy towards the divertor will increase with the plasma energy loss, which results in the sharp increase of the peak heat flux. The pitch angle on the target plates is about  $2^\circ$  near the strike point, so parallel heat flux reaches a value of  $q_{\parallel} = \frac{q_{\text{div}}}{\sin(\alpha)} = 90 \text{ MW m}^{-2}$ . The wetted areas are between  $0.5 \text{ m}^2$  and  $0.7 \text{ m}^2$ , and no clear trend of the power broadening scales with the ELM energy loss. But the ELM wetted area scales positively with ELM energy loss in JET [10]. The discrepancy may be caused by the tight baffle geometry, which is partially shadowing the divertor heat flux during ELM. During ELMs, the velocity of the radial propagation is so high that the timescale for these particles to reach plasma facing components (PFCs) at the main chamber wall is comparable with the ion transit time [8]. Investigations of ELM energy losses have

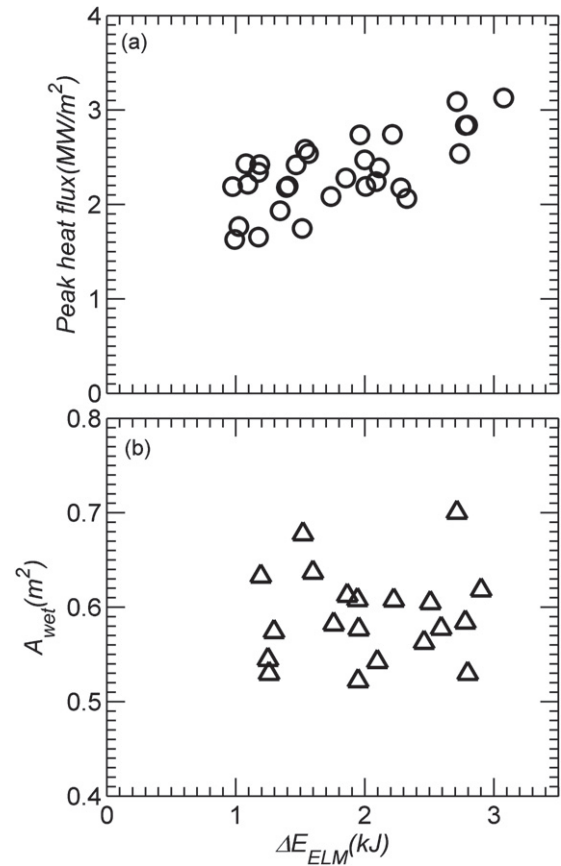


**Figure 6.** The peak heat flux (a) and the effective wetted area (b) during ELM events versus the ELM energy loss.

revealed that a non-negligible amount of the ELM energy lost by the core plasma may reach the main chamber PFCs [8, 25]. This suggests that there would be more energy deposited onto the main chamber PFCs during ELM for the closed divertor geometry. The interaction of the plasma with the baffle (see figure 1) should mainly account for this, because of the tight baffle geometry.

An integral midplane decay length is estimated with [24]:

$$\lambda_{q,\text{midplane}} = \frac{A_{\text{wet}}}{2\pi R_{\text{div}} f_x}, \quad (2)$$

here  $f_x = \frac{R_{\text{mid}} B_{\theta}^{\text{mid}}}{R_{\text{div}} B_{\theta}^{\text{div}}}$  is the poloidal magnetic flux expansion at the divertor target. The midplane integral deposited power widths of between 25 mm and 40 mm are calculated with a value of the effective flux expansion of 1.51,  $R_{\text{div}} = 1.65 \text{ m}$  for all considered discharges here.

#### 4. Energy transport in the SOL

An important aspect of the mechanism that governs the power deposition onto the target plates is the characteristic time of SOL energy transport by ELMs to the divertor. The characteristic time is estimated as collisionless transport of ions with the sound speed [23]:

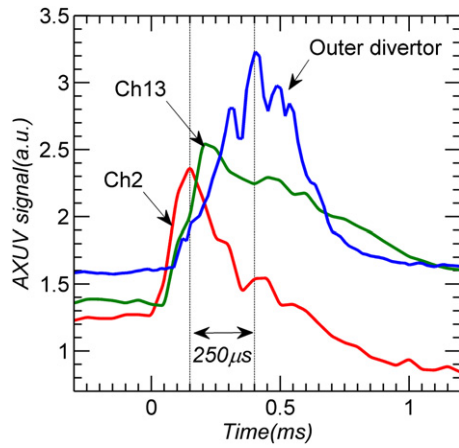


**Figure 7.** SOL poloidal propagation of ELM radiation pulse from the AXUV detector array analysis. The chordal geometry of the AXUV detector diagnostic and the lines of sight used in the analysis are defined in figure 2.

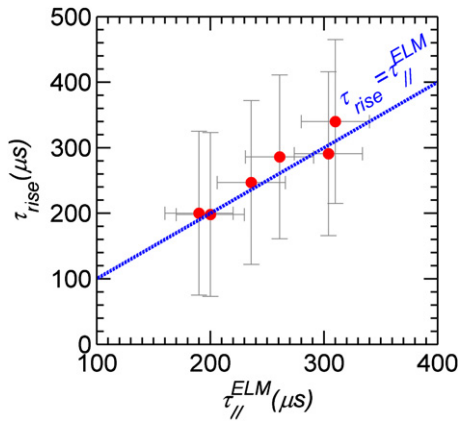


**Figure 8.** The ELM power rise time measured by IR thermography is compared to the parallel transport time of ions calculated from pedestal electron temperature.

$$\tau_{\parallel}^{\text{ELM}} = \frac{2\pi qR}{\sqrt{(T_e + T_i)/m_d}} \quad (3)$$

assuming  $T_e = T_i = T_{\text{ped}}$ ,  $T_{\text{ped}}$  is the pedestal values of electron temperature and  $m_d$  the mass of the deuterium ions. For a typical ELMy H-mode discharge in HL-2A, a connection length of about  $L = 2\pi qR = 51$  m and a pedestal temperature of about  $T_{\text{ped}} = 0.4$  keV are measured, resulting in a  $\tau_{\parallel}^{\text{ELM}} = 261$   $\mu\text{s}$ . This timescale is confirmed by the AXUV detector array data, as shown in figure 7. The radiation peak presents first in the low field side of the plasma and then in the high field side and finally in the outer divertor. These observations are consistent with SOL parallel transport from the outer midplane. The timing of the ELM induced radiation perturbation at various poloidal locations is about 250  $\mu\text{s}$  as shown in figure 7, in good agreement with ion convection parallel to SOL field lines from the midplane to the target plates. This is consistent with the results in JET by measuring soft x-ray emission and  $D_{\alpha}$  emission during ELMs [8]. The energy transport processes have been confirmed by the

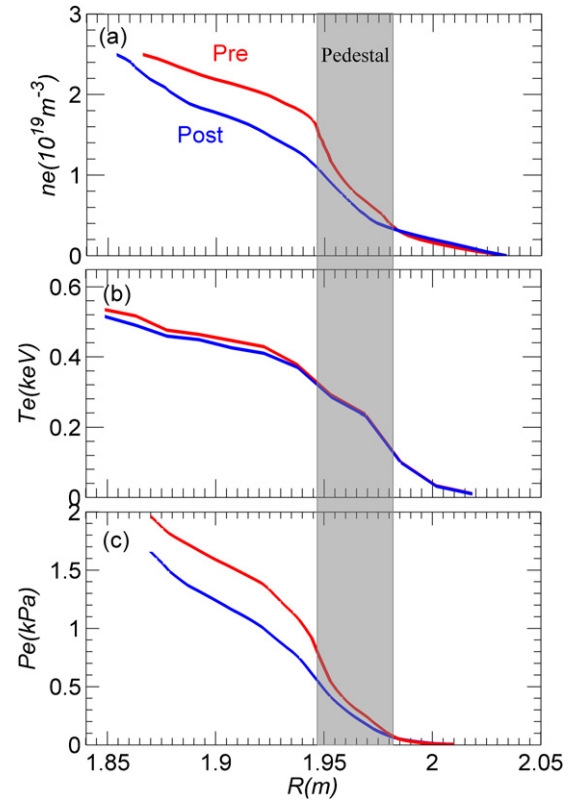


**Figure 9.** Comparison of (a) electron density, (b) electron temperature and (c) electron pressure profiles, pre- (red) and post- (blue) ELM.

timescale  $\tau_{\text{rise}}$  of the power deposition on the divertor target, as shown in figure 8. The timescale  $\tau_{\text{rise}}$  is correlated with the collisionless flight time  $\tau_{\parallel}^{\text{ELM}}$  of the pedestal energy ions to the divertor. It is consistent with results from kinetic simulations of ELMs, which indicate that a high energy sheath is formed at the ELM pedestal plasma collapse leading to the typical timescale for energy flow to the divertor being determined by ion dynamics [8]. A comparison of electron density and temperature profiles before and after the ELM (figure 9) shows that a significant drop in the density profiles is observed after ELM, while the temperature profiles look similar. This indicates that the proportion of ELM energy loss associated with the ELM density drop (ELM convective losses) is much larger than those associated with the ELM temperature drop (ELM conductive losses). Furthermore, the ELM energy deposited onto the divertor target during the decay phase is more than 70% (see figure 5), which is similar to the properties of the convective ELMs [8]. These observations may imply that convective transport along open field lines towards the divertor target dominates the parallel heat transport mechanism during ELMs. In addition, figure 9 shows that the pedestal width is about 3 cm, localized at  $\psi \sim 0.9$  (normalized poloidal flux).

## 5. ELM energy fluence scaling

### 5.1. Eich model

The peak of the ELM energy fluence profile directly relates to the material limit, which should be limited to 0.15 MJ m<sup>-2</sup> to

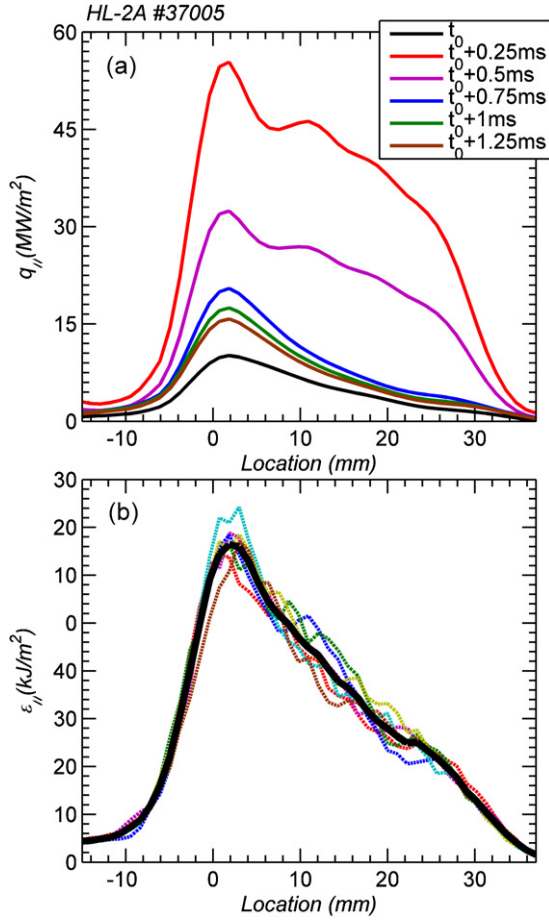


**Figure 10.** (a) Evolutions of heat flux profiles during an ELM event and (b) examples of ELM energy density profiles for seven individual ELMs on the outer divertor targets. The averaged profile (black line) is used for the ELM energy fluence scaling.

prevent edge melting [26]. The ELM energy fluence profile,  $\varepsilon_{\parallel}(s)$ , is the temporal integration of the ELM heat flux profiles over the ELM duration (defined in section 3).

$$\varepsilon_{\parallel}(s) = \int_{t_{\text{ELM}}} q_{\parallel}(s, t) dt \quad (4)$$

$$q_{\parallel}(s, t) = \frac{q_{\text{div}}(s, t) - q_{\text{div}}(s, t_0)}{\sin(\alpha_{\text{div}})} \quad (5)$$

$$\varepsilon_{\parallel}^{\text{peak}} = \max(\varepsilon_{\parallel}(s)). \quad (6)$$

The heat flux,  $q_{\text{div}}(s, t)$ , is measured by IR thermography and reduced by the heat flux just before the ELM,  $q_{\text{div}}(s, t_0)$ .  $S$  is the local coordinate along the tile surface and  $\alpha_{\text{div}}$  is the inclination angle of the field lines onto the divertor target. Figure 10 shows an example of the time evolution of the ELM heat flux profiles during an ELM event, and the ELM target energy fluence profiles for seven individual ELMs.

The Eich model provides predictions for the ELM heat loads, which are compared against a multi-machine dataset [14]. The model assumes a direct flux tube connection between the pedestal top and the divertor during an ELM, and the width of the flux tube around the pedestal top position determines the deposition area in the divertor. As mentioned in section 4, the parallel heat transport along open field lines dominates the

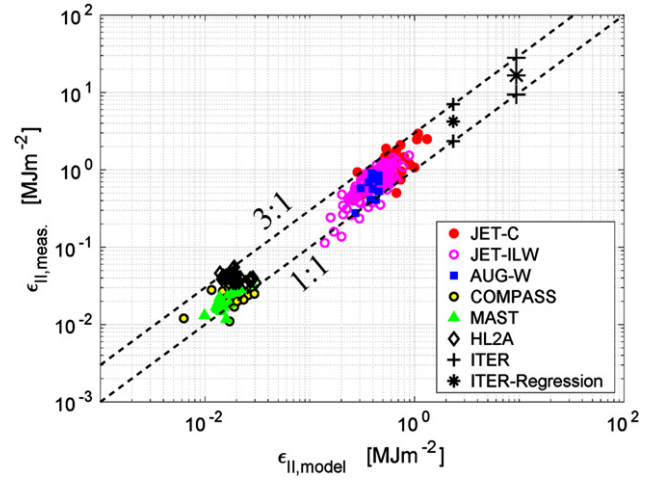


**Figure 11.** Model prediction versus the database. For comparison, the data from other devices are also shown. The dashed lines are one and three times the model prediction respectively.

transport mechanism during ELMs, so the assumption is valid for the HL-2A database. Based on the assumptions, the ELM parallel peak energy fluence is well described by the pedestal top pressure [14]:

$$\varepsilon_{\parallel} \cong 6\pi P_e R_{\text{geo}} q_{\text{edge}}. \quad (7)$$

Here,  $P_e = n_{e,\text{ped,top}} T_{e,\text{ped,top}}$  is the plasma pressure around the pedestal top region,  $q_{\text{edge}} = \sqrt{\frac{1+\kappa^2}{2}} \cdot \frac{a_{\text{geo}}}{R_{\text{geo}}} \cdot \frac{B_{\text{tor}}}{B_{\text{pol}}}$  is the edge cylindrical safety factor,  $\kappa$  is the plasma elongation,  $R_{\text{geo}}$  and  $a_{\text{geo}}$  are the geometrical major radius and minor radius, and  $B_{\text{tor}}$  and  $B_{\text{pol}}$  are the toroidal and poloidal magnetic field at the outer midplane.

## 5.2. ELM energy fluence scaling

The comparison of the experimental HL-2A data and the Eich model prediction is shown in figure 11. For comparison, the data of multi-machines are also included in the figure [14]. The experimental data range is found to lie between one and three times the model prediction, showing a good agreement with other device data. The dashed lines in figure 11 are one and three times the model prediction, and the range between two lines is possibly related to the relative ELM size [14]. The relative ELM size is defined as the ELM loss energy normalized to the plasma stored energy  $\Delta E = E_{\text{loss}}/W_{\text{plasma}}$ , which is calculated by using diamagnetic measurements on the plasma stored energy at the beginning and the end of the ELM event. Figure 12 shows the measured parallel ELM energy fluence normalized to the model prediction versus the relative ELM size. It can be seen that the data almost fill in the region between the 1:1 line and 3:1 line; data close to the 3:1 line are rare and exist only for large ELMs with relative ELM size at about 7%–9%. In addition, the distribution of the multi-machines database demonstrates a relationship between the parallel ELM energy fluence and the relative ELM size,  $\varepsilon_{\parallel} \sim \Delta E^{\alpha}$  with  $\alpha$  being between 0 and 1, which is consistent with the regression studies report of  $\varepsilon_{\parallel} \sim \Delta E^{0.5}$  [14].



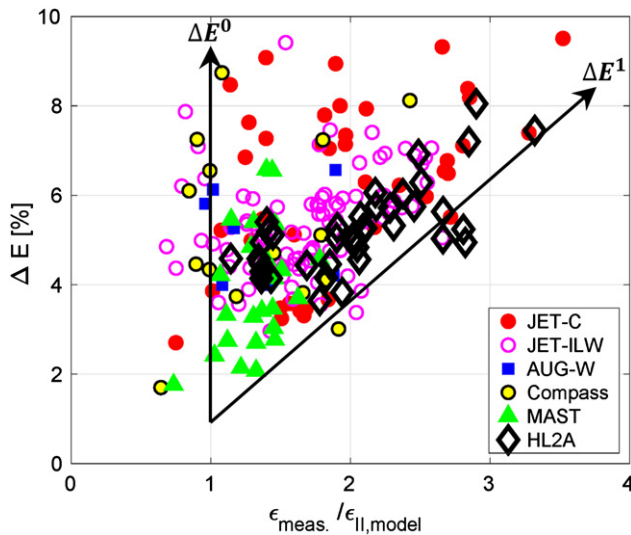


**Figure 12.** The distribution of the relative ELM size versus the measured parallel ELM energy fluence normalized to the model prediction.

However, there is a significant scatter in the HL-2A dataset, which may be because of ELMs with large convective transport (see section 4) near the L-H threshold, as the interpretation in DIII-D [16]. The DIII-D results show that the prediction of Eich's model is more accurate when the heating power is much larger than the L-H power threshold, while the predicted values,  $\varepsilon_{||}$ , are underestimated for the ELM near the L-H power threshold [16]. In HL-2A, the heating power is not very large and close to the L-H threshold power. In this case, if the peak ELM energy density values are underestimated, the uncertainty in the ratio,  $\varepsilon_{\text{meas.}}/\varepsilon_{||,\text{model}}$ , will increase, resulting in the large scatter in HL-2A dataset. However, the ratio of  $\frac{P_{\text{Heat}}}{P_{\text{LH}}}$  in HL-2A is in the range of 1.6 to 2.2, and the distribution of the measured relative ELM energy density to Eich model prediction is almost equally filled in this range. No clear tendency was found over the very limited range of  $\frac{P_{\text{Heat}}}{P_{\text{LH}}}$ . Here the heating power,  $P_{\text{heat}}$ , is the sum of ohmic and external heating by NBI. The L-H threshold power,  $P_{\text{LH}}$ , is defined by [27]:

$$P_{\text{LH}} = 0.049 \bar{n}_e^{-0.72} B_T^{0.8} S^{0.94}. \quad (8)$$

Here  $\bar{n}_e$  stands for the line-averaged electron density in  $10^{20} \text{ m}^{-3}$ ,  $B_T$  for magnetic field strength in T, and  $S$  for the plasma surface in  $\text{m}^2$ .

## 6. Summary and conclusions

A set of ELMy H-mode discharges has been optimized for ELM energy deposition studies. Insight into the temporal or spatial evolution of the ELM structure is gained by a statistical analysis of the amplitudes and spatial distribution of the pattern on the divertor targets. The ELM energy loss in HL-2A is about 3%–8% of the plasma stored energy, and the corresponding peak heat flux and the integrated power decay length are in

the range of 1.5–3.2  $\text{MW m}^{-2}$  and 25–40 mm, respectively. The observed rise times are between about 200  $\mu\text{s}$  to 400  $\mu\text{s}$ , and the decay times are typically 1.5 to 4 times longer than the corresponding rise times, but the fraction of the ELM energy loss deposited onto the divertor targets during rise phase is less than about 30%. Furthermore, during ELMs the peak heat flux increases with ELM energy loss while the wetted areas show no clear trend with the ELM energy loss, which may be caused by the interaction of the plasma and the PFCs due to the closed divertor geometry.





A characterization of the ELM pedestal losses separately in temperature and density has revealed both conductive as well as convective ELM losses for DIII-D [28], JET [29] and ASDEX Upgrade [30]. But the conductive energy loss tends to decrease at higher collisionality [8], even to a very low level near the L-H threshold [16]. The observations in HL-2A show that the ELM power rise time scales with the convective parallel time, therefore, ELMs are expected to have mainly convective transport properties. A delay in the response of the divertor plasma radiation of the ELM perturbation relative to pedestal radiation is observed as expected for the convective transport of energy. The evolutions of electron density and temperature profiles before and after ELMs also suggest the convective fraction is much larger than the conductive part.

The convective transport along open field lines towards the divertor target dominates the parallel heat transport mechanism during ELMs. This observation supports the Eich model assumption of a direct flux tube connection between the pedestal top and the divertor during an ELM. Finally, the ELM energy,  $\varepsilon_{||}$ , is compared with the predictions of the model, and it shows a good agreement between experimental and predicted values on HL-2A. It should be noted that the HL-2A tokamak is operated with very closed divertor geometry compared with other open divertor geometries. Furthermore, a nearly circular plasma configuration is also very different to that with high triangularities in other devices. However, there are no clear effects of these different elements on the Eich model, and a good agreement between these different devices is observed although there is a signature scatter in the HL-2A data.

## Acknowledgments

This work was supported by the National Key R&D Program of China under Grant Nos. 2018YFE0303101, 2017YFE0301106, 2017YFE0301202, 2019YFE03030002 and 2018YFE0310300, and the Natural Science Foundation of China under Grant Nos. 11875020 and 11875023. This work has been part funded by the EPSRC Grant EP/T012250/1.

## ORCID iDs

T. Eich  <https://orcid.org/0000-0003-3065-8420>  
 J. Adamek  <https://orcid.org/0000-0001-8562-1233>  
 N. Wu  <https://orcid.org/0000-0001-7949-5330>  
 L.M. Yu  <https://orcid.org/0000-0002-1177-3063>

## References

- [1] Loarte A. et al 2007 Progress in the ITER physics basis chapter 4: power and particle control *Nucl. Fusion* **47** S203
- [2] Pitts R.A. et al 2017 *Nucl. Mater. Energy* **12** 60
- [3] Pitts R.A. et al 2019 *Nucl. Mater. Energy* **20** 100696
- [4] Wagner F. et al 1982 *Phys. Rev. Lett.* **49** 1408
- [5] Zohm H. 1996 *Plasma Phys. Control. Fusion* **38** 105
- [6] Sieglin B., Faitsch M., Eich T., Herrmann A. and Suttrop W. 2017 *Phys. Scr.* **T170** 014071
- [7] Pitts R.A., Andrew P., Arnoux G., Eich T., Fundamenski W., Huber A., Silva C. and Tskhakaya D. 2007 *Nucl. Fusion* **47** 1437
- [8] Loarte A., Saibene G. and Sartori R. 2004 *Phys. Plasmas* **11** 2668
- [9] Eich T., Andrew P., Herrmann A., Fundamenski W., Loarte A. and Pitts R.A. (JET-EFDA Contributors) 2007 *Plasma Phys. Control. Fusion* **49** 573
- [10] Eich T., Thomsen H., Fundamenski W., Arnoux G., Brezinsek S., Devaux S., Herrmann A., Jachmich S. and Rapp J. 2011 *J. Nucl. Mater.* **415** S856
- [11] Eich T. et al 2005 *Plasma Phys. Control. Fusion* **47** 815
- [12] Fenstermacher M.E. et al 2003 *Plasma Phys. Control. Fusion* **45** 1597
- [13] Wang L. et al 2013 *Nucl. Fusion* **53** 073028
- [14] Eich T., Sieglin B., Thornton A.J., Faitsch M., Kirk A., Herrmann A. and Suttrop W. 2017 *Nucl. Mater. Energy* **12** 84
- [15] Adamek J. et al 2017 *Nucl. Fusion* **57** 116017
- [16] Knolker M. et al 2018 *Nucl. Fusion* **58** 096023
- [17] Duan X.R. et al 2010 *Nucl. Fusion* **50** 095011
- [18] Gao J.-M., Li W., Xia Z.-W., Pan Y.-D., Lu J., Yi P. and Liu Y. 2013 *Chin. Phys. B* **22** 015202
- [19] Eich T. et al 2013 *Nucl. Fusion* **53** 093031
- [20] Zhong W.L. et al 2014 *Rev. Sci. Instrum.* **85** 013507
- [21] Shi Z.B. et al 2014 *Rev. Sci. Instrum.* **85** 023510
- [22] Pitts R.A., Alberti S., Blanchard P., Horacek J., Reimerdes H. and Stangeby P.C. 2003 *Nucl. Fusion* **43** 1145
- [23] Eich T. et al 2005 *J. Nucl. Mater.* **337–339** 669
- [24] Loarte A. et al 1999 *J. Nucl. Mater.* **266–269** 587
- [25] Herrmann A., Eich T., Rohde V., Fuchs C.J. and Neuhauser J. (ASDEX Upgrade Team) 2004 *Plasma Phys. Control. Fusion* **46** 971
- [26] Gunn J.P. et al 2017 *Nucl. Mater. Energy* **12** 75
- [27] Martin Y.R. and Takizuka T. (the ITPA CDBM H-mode Threshold Database Working Group) 2008 *J. Phys.: Conf. Ser.* **123** 012033
- [28] Leonard A.W., Groebner R.J., Mahdavi M.A., Osborne T.H., Fenstermacher M.E., Lasnier C.J. and Petrie T.W. 2002 *Plasma Phys. Control. Fusion* **44** 945
- [29] Loarte A. et al 2003 *Plasma Phys. Control. Fusion* **45** 1549
- [30] Urano H., Suttrop W., Horton L.D., Herrmann A. and Fuchs J.C. (ASDEX Upgrade Team) 2003 *Plasma Phys. Control. Fusion* **45** 1571